Multimodal imaging combining time-domain near-infrared optical tomography and continuous-wave fluorescence molecular tomography

Ren, Wuwei; Jiang, Jingjing; Di Costanzo Mata, Aldo; Kalyanov, Alexander; Ripoll, Jorge; Lindner, Scott; Charbon, Edoardo; Zhang, Chao; Rudin, Markus; Wolf, Martin

DOI
10.1364/OE.385392

Publication date
2020

Document Version
Final published version

Published in
Optics Express

Research Article Vol. 28, No. 7 / 30 March 2020 / Optics Express 9860
Optics EXPRESS

Multimodal imaging combining time-domain near-infrared optical tomography and continuous-wave fluorescence molecular tomography

WUWEI REN,[1,2,*] JINGJING JIANG,[1] ALDO DI COSTANZO MATA,[1] ALEXANDER KALYANOV,[1] JORGE RIPOLL,[3,4] SCOTT LINDNER,[1,5] EDOARDO CHARBON,[5] CHAO ZHANG,[6] MARKUS RUDIN,[2] AND MARTIN WOLF[1]

[1]*Biomedical Optics Research Laboratory, University Hospital Zurich, 8091 Zurich, Switzerland*
[2]*Institute for Biomedical Engineering, University of Zurich & ETH Zurich, 8093 Zurich, Switzerland*
[3]*Department of Bioengineering and Aerospace Engineering, Universidad Carlos III de Madrid, 28911 Leganés, Madrid, Spain*
[4]*Instituto de Investigación Sanitaria Gregorio Marañón, 28007 Madrid, Spain*
[5]*Advanced Quantum Architectures Lab, École Polytechnique Fédérale de Lausanne, 2002 Neuchâtel, Switzerland*
[6]*Department of Quantum and Computer Engineering, Delft University of Technology, 2628 Delft, Netherlands*
[*]*ren@biomed.ee.ethz.ch*

Abstract: Fluorescence molecular tomography (FMT) emerges as a powerful non-invasive imaging tool with the ability to resolve fluorescence signals from sources located deep in living tissues. Yet, the accuracy of FMT reconstruction depends on the deviation of the assumed optical properties from the actual values. In this work, we improved the accuracy of the initial optical properties required for FMT using a new-generation time-domain (TD) near-infrared optical tomography (NIROT) system, which effectively decouples scattering and absorption coefficients. We proposed a multimodal paradigm combining TD-NIROT and continuous-wave (CW) FMT. Both numerical simulation and experiments were performed on a heterogeneous phantom containing a fluorescent inclusion. The results demonstrate significant improvement in the FMT reconstruction by taking the NIROT-derived optical properties as prior information. The multimodal method is attractive for preclinical studies and tumor diagnostics since both functional and molecular information can be obtained.

1. Introduction

Fluorescence molecular tomography (FMT) copes with the highly scattering nature of living tissues and resolves fluorescence signals at a depth of several centimeters, making it a powerful non-invasive imaging tool for preclinical studies [1,2]. With the proper selection of clinically proved contrast agents, such as indocyanine green (ICG), FMT holds a promising future for clinical applications. Feasibility studies were reported in clinical fields including breast cancer diagnostics [3], screening finger synovitis [4], and image-guided surgery [5]. Apart from the influence of hardware factors such as detector sensitivity and laser stability [6], image reconstruction plays a pivotal role in determining spatial resolution, accuracy, and robustness of final tomographic images. The reconstruction algorithm of FMT consists of two steps, i.e., forward modeling for predicting the light propagation in biological tissue and inversion for recovering the fluorescence distribution from the acquired raw data [7]. For the first step, the diffusion equation (DE) is commonly used to describe the light propagation in highly turbid

#385392 https://doi.org/10.1364/OE.385392
Journal © 2020 Received 16 Dec 2019; revised 16 Feb 2020; accepted 2 Mar 2020; published 23 Mar 2020

Optics EXPRESS

media considering both absorption and scattering effects [8]. The DE can be solved by using either analytical methods by deriving the Green function [8] or numerical ways such as boundary element method (BEM) [9] and finite element method (FEM) [10]. More recently, Monte Carlo methods have been also applied in FMT reconstruction [11,12]. A comprehensive overview of inversion techniques may be found in reviews such as [7,13].

One of the most challenging problems associated with FMT reconstruction is that both forward modeling and subsequent inversion depend largely on the assumed optical properties [14]. The most straightforward way to address the problem is by assuming a homogeneous setting of optical properties, which in principle mimics the average optical values of tissue in-vivo. This method is typically used in the FMT reconstruction based on an analytical solution [1]. However, it is intuitive to foresee that the assumption of homogeneity can cause inaccuracy, especially when encountering a highly heterogeneous sample such as a mouse head. Normalized Born (nBorn) approximation, a widely accepted ratiometric method in FMT, normalizes fluorescence signal with respect to the signal at excitation wavelength [15]. nBorn approximation accounts for the heterogeneity of absorption to a certain degree but is less effective concerning the heterogeneity of scattering [14,16]. Optical properties may be attributed to specific tissues by combining FMT with another high-resolution imaging method, such as X-ray computed tomography (CT) or magnetic resonance imaging (MRI), which serves as a structural reference [3,17–21]. The acquired structural image is segmented into different regions, each characterized by a specific property value. Nevertheless, two new issues arise with this multimodal imaging method: 1) The optical map is not directly correlated with the CT or MRI images. The segmentation based on those images does not capture the complexity of tissue, i.e., segmented regions still display heterogeneity. 2) there is no consensus in the literature on the true optical properties for different types of living tissues [22,23]. This disagreement can be found in both absorption and scattering coefficients [23]. Moreover, the intersubject variation of tissue-specific optical properties is considerable [22,24].

A more direct way to find the missing information is by estimating the optical parameters from near-infrared optical tomography (NIROT) (also referred to diffuse optical tomography, or DOT) [7,25]. Tan et al. have demonstrated that the NIROT-derived optical properties play a critical role in improving quantitative FMT using FEM-based reconstruction, with systematic simulation/phantom validation [26] and an in vivo pilot study on a tumor animal model [27]. The optical properties can be more accurately reconstructed using structural a priori information [28]. Ducros et al. use NIROT to derive a so-called optical inhomogeneity map, a modified version of the optical property, by considering both absorption and scattering coefficients. A two-step NIROT-FMT reconstruction strategy has been proposed to generate a more robust result in both simulation and phantom experiments [29]. All the reported NIROT-FMT methods so far were implemented only with the continuous-wave (CW) mode. However, in CW-NIROT, it is mathematically challenging to obtain both the values of absorption and scattering coefficients simultaneously [30]. Additional information to mere intensity measurement is required to unmix the absorption and scattering coefficients effectively. The time-domain method yields this additional information by providing measures for both the intensity and arrival time of photons. More interestingly, a more accurate depiction of optical properties not only improves FMT reconstruction but also provides additional functional information on hemodynamics and local blood oxygenation, relevant for characterizing the physiological state of the tissue. Those functional information are valuable for studies, e.g., brain functioning and cancer diagnostics [31,32].

Recently we have developed a new-generation TD-NIROT by integrating the state-of-the-art single-photon avalanche diodes (SPAD) camera with 116 ps time response [33]. The SPAD camera has 32 x 32 pixels with a fill factor of 28%, leading to an enormous number of 1024 TD detectors [34]. Compared to CW-NIROT and traditional TD-NIROT using bulky

Optics EXPRESS

photomultipliers, the new NIROT with SPAD technology provides more source-detector pairs and, consequently, more accurately recovered optical properties. It also enables non-contact measurements and is simple to integrate into other optical imaging modalities, such as FMT. In this work, we have developed a multimodal imaging strategy by using the novel TD-NIROT and a previously reported CW-FMT system [19,35]. Both NIROT and FMT measurements were conducted on a semitransparent cylindrical phantom with an optical heterogeneity and a fluorescent inclusion. FMT reconstruction using experimental and simulated datasets was performed under the assumption with several different sets of optical properties, including the NIROT-derived values. In the end, the resulted fluorescence signals were evaluated and compared using several quantitative metrics. The aim of that was to evaluate how a combination of FMT with TD-NIROT improves the reconstruction accuracy of FMT.

2. Methods

2.1. Theoretical background

Both NIROT and FMT work in the diffusive regime of light propagation. With photon density distribution $\phi(r,t)$ at position r and time point t, it can be described by the time-dependent DE as below:

$$[-\nabla\cdot\kappa(r)\nabla+\mu_a(r)+\frac{1}{c}\frac{\partial}{\partial t}]\phi(r,t)=q(r,t)\quad r\in\Omega \tag{1}$$

with a boundary condition as:

$$\phi(r,t)+2\zeta(c)\kappa(r)\frac{\partial\phi(r,t)}{\partial\nu}=0\quad r\in\partial\Omega \tag{2}$$

where q is a source term caused by external illumination or internal fluorescence. The model parameters include absorption coefficient μ_a, diffusion coefficient $\kappa=[3(\mu_a+\mu_s)^{-1}]$ with reduced scattering coefficient μ_s, and speed of light c. The boundary condition contains the refractive index mismatch ζ, the outward boundary normal $\partial\nu$.

In the case TD-NIROT, a pulsed laser source $q_{\text{nirot}}(r,t)$ is introduced and the resulted $\phi_{\text{nirot}}(r,t)$ can be solved by directly applying Eq. (1).

$$[-\nabla\cdot\kappa(r)\nabla+\mu_a(r)+\frac{1}{c}\frac{\partial}{\partial t}]\phi_{\text{nirot}}(r,t)=q_{\text{nirot}}(r,t) \tag{3}$$

On the other hand, our FMT utilizes CW laser without considering the time variable. A typical FMT experiment consists of coupled excitation and emission procedures, leading to the following paired DEs:

$$[-\nabla\cdot\kappa^{\text{ex}}(r)\nabla+\mu_a^{\text{ex}}(r)]\phi_{\text{fmt}}^{\text{ex}}(r)=q_{\text{fmt}}(r) \tag{4}$$

$$[-\nabla\cdot\kappa^{\text{em}}(r)\nabla+\mu_a^{\text{em}}(r)]\phi_{\text{fmt}}^{\text{em}}(r)=\eta C(r)\phi_{\text{fmt}}^{\text{ex}}(r) \tag{5}$$

Here, during the excitation phase Eq. (4), the source term on the right side of the equation denotes the CW light source, while for the emission phase Eq. (5), this term changes to the internal fluorescence given by the product of an efficiency constant η, unknown fluorescence concentration $C(r)$, and excited photon density $\phi_{\text{fmt}}^{\text{ex}}(r)$. In the following, we neglect the difference of μ_a, μ_s, and κ for different wavelengths at excitation and emission phases.

The inverse problem can be solved by minimizing an objective function Ψ_{mod} containing a term for discrepancy between measured and simulated data, and a regularization term:

$$\Psi_{\text{mod}}(x)=\frac{1}{2}\sum_i[y_{i,\text{mod}}-f_{i,\text{mod}}(x)]^2+\tau\mathcal{R}(x)\quad \text{mod}\in\{\text{nirot},\text{fmt}\} \tag{6}$$

For different modalities, the definition of the unknown x, the detected value y, the forward model f differs. In TD-NIROT, we aim at solving the 3D distribution of unknown optical scattering and

Optics EXPRESS

aborsption coefficients, i.e. $x = \{\mu_a(r), \mu_s(r)\}$. The ith measurement value $y_{i,\text{nirot}}$ is determined by the boundary photon density value $\phi_{\text{nirot}}(r,t)|_{\partial\Omega}$ and the detector reponse. $f_{i,\text{nirot}}$ is determined by the time-dependent DE (Eq. (3)). In the case of CW-FMT, the unknown is the spatial distribution of fluorescent dye, i.e. $x = C(r)$. Measured $y_{i,\text{fmt}}$ is a normalized value by taking the ratio of $\phi^{\text{em}}_{\text{fmt}}|_{\partial\Omega}$ between $\phi^{ex}_{fmt}|_{\partial\Omega}$, which is also associated with the detector response. $f_{i,\text{fmt}}$ accounts for both excitation and emission phases of an FMT experiment, which are given by Eqs. (4) and (5) respectively. In both modalities, we applied Tikhonov regularization in $\mathcal{R}$, tuned by a hyperparameter τ.

We discretize the forward model using a Galerkin FEM once the object is meshed into tetrahedral elements. In TD-NIROT, the time derivative term can be approximated by a finite-difference scheme. The details for FEM formulation and inversion are referred to [19].

For FMT, the dependency of $y_{i,\text{fmt}}$ on the optical properties of tissue can be approximated [16]:

$$y_{i,\text{fmt}} \propto \mu_s exp(-\sqrt{3\mu_a\mu_s R_{corr}}) \tag{7}$$

where R_{corr} is a correction parameter depending the locations of detector and light source. Equation (7) indicates that μ_a and μ_s have different weights to the measurement y and thus affect the final reconstruction quality unequally. We will investigate this problem by assigning different combinations of scattering and absorption coefficients in a series of reconstrcution cases in section 2.4.

2.2. Phantom design, fabrication, and calibration

For both simulation and experiments, we have designed a cylindrical silicone phantom with heterogeneous optical properties (Fig. 1). The phantom has a radius of 30 mm and a height of 20 mm, with a dark block inclusion with a higher absorption coefficient and scattering coefficient similar to the surrounding material. We used material A to produce the bulk of the phantom and material B to produce the inner block. Both material A and B are based on the silicone matrix (Silpuran 2420, Wacker, Germany). We achieved different levels of absorption by applying various mixtures of added ink [36]. Material A contains carbon black powder for absorption and white pigment (RAL 9010, Wacker, Germany) for scattering, whereas material B includes additional ink (RAL 6004, Wacker, Germany) to enhance the absorption. Additionally, there is a tube passing through the center of the inner block that allows the injection of the fluorescence dye.

For validation purposes, we calibrated the optical properties of material A and B using frequency-domain near-infrared spectroscopy (Imagent, ISS Inc, US, IL). The spectroscopy utilized a self-calibrating probe [37] to measure absolute values of μ_a and μ_s at 4 wavelengths: 689, 725, 802 and 838 nm. Implementation of the self-calibrating method imposes certain limitations on the system arrangement since the method requires a semi-infinite homogeneous geometry of the object. Therefore, we cast two homogeneous phantoms with material A and B, respectively. These homogeneous phantoms were cast in a cylindrical shape (radius, 120 mm; height, 60 mm), thus been large enough to fulfill the semi-infinite boundary condition. As we will use cyanine 5.5 (Cy5.5) as the fluorescence dye with peak absorption at 680 nm and peak emission at 710 nm, we adopted the values measured at the wavelength of 689 nm. The calibrated values for absorption and scattering are {0.0053, 0.97} mm^{-1} for material A and {0.033, 0.89} mm^{-1} for material B.

2.3. Near-infrared optical tomography

The NIROT system (Fig. 2(a)) uses a supercontinuum laser (Fianium WL-SC-480-8, NKT, Denmark) as the illumination source, which is guided through a fiber switch (Laser Components, Germany) to 11 fibers [33]. These fibers are integrated into a customized source ring (radius,

Optics EXPRESS

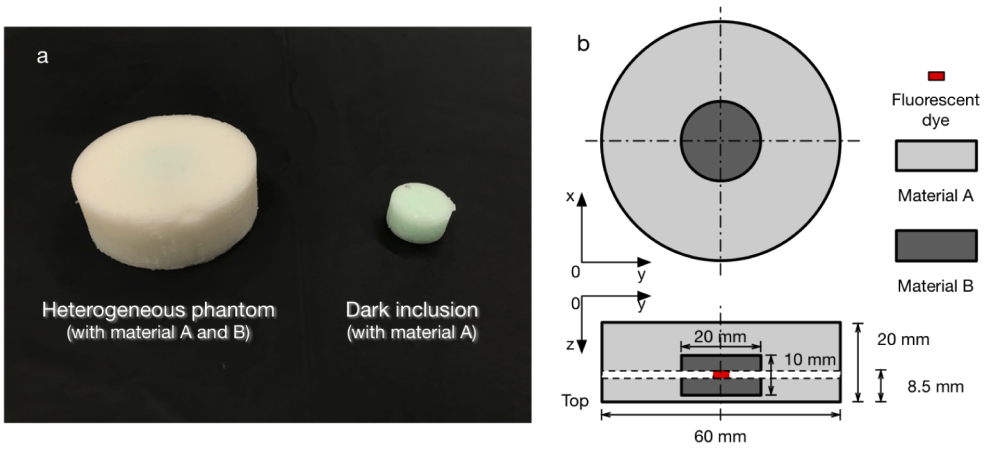

Fig. 1. An optically heterogeneous phantom was fabricated by mixing silicone gel with carbon black and titanium dioxide to generate different levels of absorption and scattering (materials A & B). The phantom is cylindrical with a radius of 30 mm and a height of 20 mm. There is a dark block inclusion at 8.5 mm depth below the top surface. Fluorescent dye (red) is allowed to injected in the center the block for the FMT measurement.

22.5 mm) to be placed on the sample surface. The 32 x 32 SPAD camera is mounted on the source ring equipped with a transparent window and an ultra-wide lens (focal length, 1.7 mm; NA, 1.8; MY110M, Theia Technologies, Japan). The in-house-built SPAD camera is capable of capturing 224 M events/s and achieves a photon detection efficiency of about 7% at 710 nm wavelength [34]. The whole NIROT system covers 25 x 25 mm^2 field of view and is operated in a reflection mode, i.e., the illumination and detection placed on the same side. During the experiment, a pulsed laser at the wavelength of 689 nm was used, and for each source fiber, the measurement took approximately 50 s for each source, resulted in a total measurement time of 9 min. A FEM-based simulator is utilized to model the light transport [38]. The measured TD data was transformed into the frequency domain with MATLAB FFT function and sampled at several selected frequencies for image reconstruction where a Newton-like iterative process is taken to update the optical properties [39].

2.4. *Fluorescence molecular tomography*

We performed the FMT experiment with our in-house-built system (Fig. 2(b)). The system incorporates a 16-bit CCD camera (ANDOR, Belfast, Northern Ireland) with 1024 x 1024 pixels at a working temperature of -80 °C to reduce the dark noise. The CW illumination is generated by a solid-state laser (B&W Tek, Newark, USA) at a wavelength of 670 nm. The laser beam is further directed by a galvanometric driven mirror system (Scancube, ScanLab, Puchheim, Germany) to project it onto the phantom surface. We applied a transmission-mode FMT by illuminating the bottom of the phantom with 8 x 8 laser points and acquired the paired excitation and emission images from the top surface for each laser point. We chose the filters at wavelengths of 680 and 710 nm for excitation and emission images respectively.

For FMT reconstruction, we used a modular software platform (*STIFT*) [19] with integrated modular functions, including meshing (by calling *iso2mesh* [40]), forward modeling (by calling *TOAST++* [41]), various inversion and visualization methods. According to the geometry of the cylindrical phantom, a tetrahedral mesh was generated for FEM modeling. The mesh contains 12230 nodes, 72823 tetrahedral elements, and 3484 surface triangular elements. Figure 3 shows the problem setting for reconstructing an experimental dataset. The detection plane

Optics EXPRESS

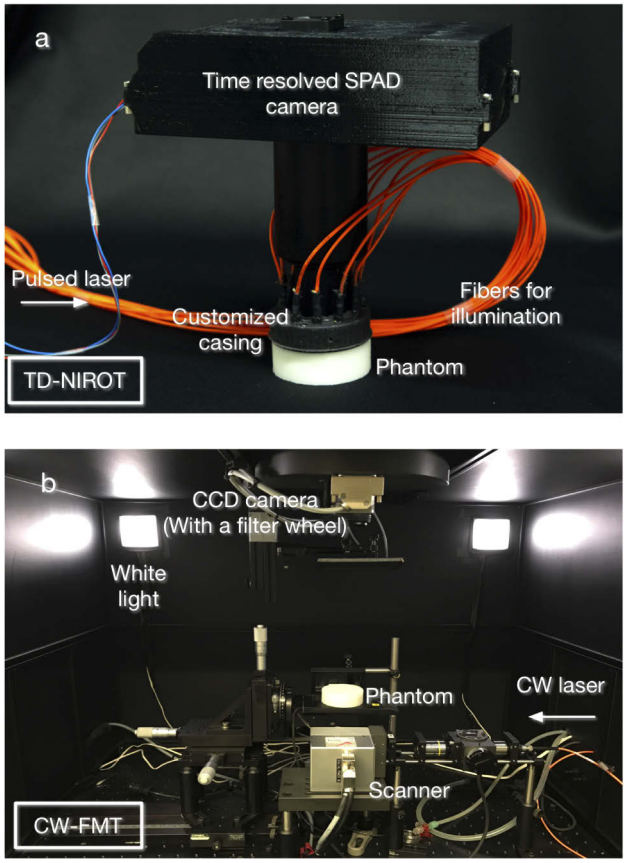

Fig. 2. (a) The TD-NIROT system incorporates an in-house-built 32 x 32 SPAD camera and 11 optical fibers for illumination. (b) The CW-FMT system uses a highly sensitive CCD camera for fluorescence detection and applies non-contact measurement in a transmission mode.

was resampled, forming a 41 x 41 detection array (blue patches). The positions of 8 x 8 laser sources were registered using a white-light image (Fig. 3, right) and attached to the mesh surface (red dots). A grid containing 29 x 29 x 11 voxels are used for reconstruction. The problem setting for simulated data reconstruction is identical to the setting above except that assigning the illumination points does not require registration with the white-light image.

To investigate the importance of introducing a correct map of optical properties for the final performance of FMT reconstruction, different combinations of scattering and absorption coefficients were used as the prior information for reconstruction. Table 1 indicates the reference of a specific optical property in different reconstruction tasks (C1-C5). The suffix of '-S' or '-E' denotes the dataset is obtained from simulations or real experiments. 'Calibration' means that the value is from calibrated values (see section 2.2). In the 'Estimation' case, both absorption and scattering coefficients were approximately twice as the values for material B, with μ_a = 0.06 mm^{-1} and μ_s = 2 mm^{-1}. For C5-S/E, the values were obtained from TD-NIROT. For the inversion, the regularization parameter τ was set to 5 x 10^{-3}. The maximum number of iterations was 100, with an error tolerance of 10^{-5}. All codes were implemented with MATLAB (R2019a, MathWorks, US) on a computer with Intel core i7@ 2.60 GHz and RAM of 8.00 GB.

Optics EXPRESS

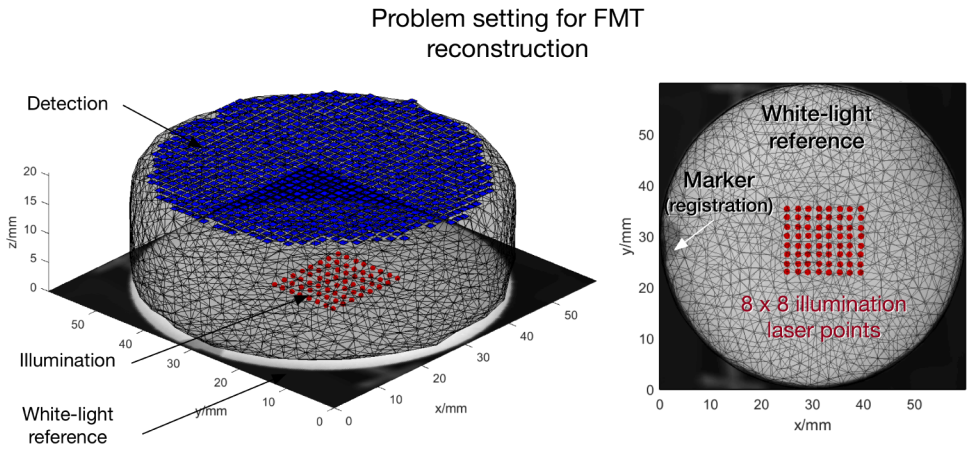

Fig. 3. The left image shows the basic problem setting for reconstructing an experimental dataset. A 41 x 41 virtual array was used for detection (blue patches), and a grid of 8 x 8 laser points for illumination (red dots). Pixels outside the sample surface were hidden. The right image shows the illumination points and the white-light image of the phantom, which was used for image registration.

Table 1. FMT reconstruction using different maps of optical properties (mm^{-1})

Case	μ_a Source	$\mu_{a,A}$	$\mu_{a,B}$	μ_s Source	$\mu_{s,A}$	$\mu_{s,B}$
C1-S/E	Calibration	0.0053	0.033	Calibration	0.97	0.89
C2-S/E	Calibration	0.0053	0.033	Estimation	2	2
C3-S/E	Estimation	0.06	0.06	Calibration	0.97	0.89
C4-S/E	Estimation	0.06	0.06	Estimation	2	2
C5-S/E	TD-NIROT	-	-	TD-NIROT	-	-

2.5. Evaluation

In order to analyze quantitatively the reconstruction results using different maps of optical properties, we adopted three widely used metrics: Mean square error (MSE), Dice similarity (Dice), and Contrast to noise ratio (CNR). We used those metrics to compare the reconstructed image x and the ground truth x^* after defining a region of interest (ROI), the set of entries that have intensity greater than a threshold, which we defined as half of the maximum intensity. N denotes the dimension of x and x^*. In other words, $\mathrm{ROI}(x) = \{x_i : x_i > \frac{1}{2}\max\{x\}, i = 1, \ldots, N\}$. The three metrics are defined as follows:

- MSE describes the general deviation of the reconstruction result from the ground truth. A smaller MSE indicates less deviation from the ground truth, i.e. a better reconstruction

$$\mathrm{MSE} = \frac{1}{N}\sum_{i=1}^{N}(x_i - x_i^*)^2 \tag{8}$$

- Dice similarity between the reconstructed ROI and the true ROI measures the shape and location accuracy of the reconstructed image. The Dice value ranges from 0 to 1, with 1 representing a complete overlap between x and x^* (i.e., a perfection geometric reconstruction). Here, $|\cdot|$ denotes the cardinality of a set.

$$\mathrm{Dice} = \frac{2|\mathrm{ROI}(x) \cap \mathrm{ROI}(x^*)|}{|\mathrm{ROI}(x)| + |\mathrm{ROI}(x^*)|} \tag{9}$$

Optics EXPRESS

- CNR expressed in decibels (dB) measures how well the reconstructed image is distinguished from the background noise:

$$\mathrm{CNR}(x) = 10\log_{10}\left\{\frac{\sum_{i=1}^{N}(x_i^*)^2}{\sum_{i=1}^{N}(x_i - x_i^*)^2}\right\} \tag{10}$$

3. Results

3.1. Reconstructed optical properties from NIROT

Compared with CW-NIROT, TD-NIROT has the advantage to decouple both absorption and scattering coefficients without assuming either of them. In Fig. 4, xy-, yz-, and xz-planes for μ_a and μ_s are visualized at the cross position of (30,30,11) mm. Both optical properties reveal the heterogeneity introduced by the inclusion in the middle. The average recovered absorption inside the dashed line is approximately 3 times that of the surrounding, while the average scattering value is 1.2 times compared to the surrounding. Considering the system error caused by the instrument for calibration, the absolute values of NIROT-derived optical properties agree well with the calibrated values within an acceptable variation.

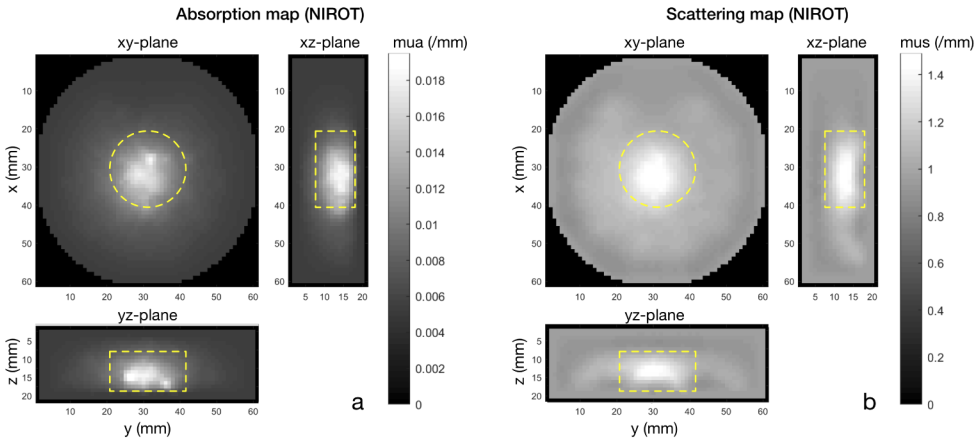

Fig. 4. Both absorption (a) and scattering (b) coefficients of the cylindrical phantom can be recovered via TD-NIROT. Three planes are visualized at the cross position of (30, 30, 11) mm for each coefficient. The dashed yellow lines indicate the true position of the dark block inclusion.

3.2. FMT reconstruction from simulated data

To understand the influence of loading different combinations of optical properties into the FMT reconstruction, we firstly conducted a numerical simulation. In the *STIFT* platform, we applied calibrated optical properties for the forward modeling and generated simulated measurement datasets for reconstruction. 5% noise level was added to the simulated measurement data. In the later step of inversion, we calculated a different weighting matrix for each case of reconstruction tasks (C1-C5), by using the specific combination of optical properties according to Table 1. In the following Fig. 5, all three planes of reconstructed fluorescence signals are displayed. Intuitively, C1-S (Fig. 5(b)) clearly shows the best result as it utilized the identical optical properties as the forward modeling. The reconstruction quality of C2/C3/C4-S (Figs. 5(c)–5(e)) is degraded because 'wrong' optical properties were used for reconstruction. Among these three cases, C2-S outperforms C3-S and C4-S, with a visually strong contrast of fluorescence signal at the correct

Optics EXPRESS

centered position of the phantom, although the signal is more blurred compared with C1-S. C5-S, which is reconstructed using NIROT-derived optical properties, shows significant improvement compared with C2/C3/C4-S and shares a similar visual quality with C1-S.

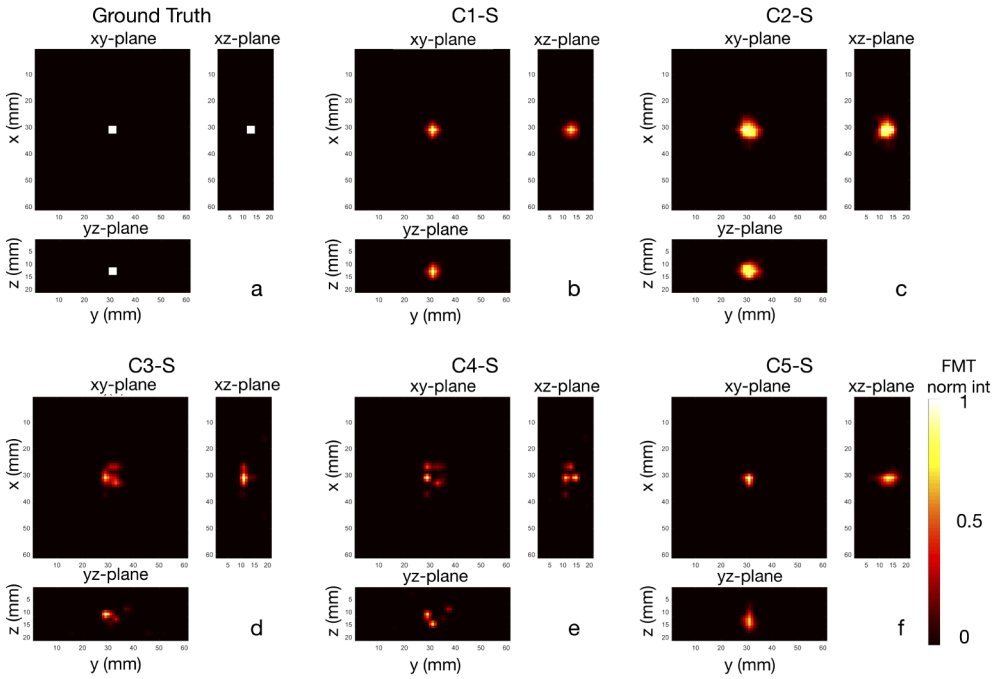

Fig. 5. The reconstructed fluorescence distributions from simulated data using different maps of optical properties (b-f) are compared with the ground truth (a). C1-S, C2/3/4-S, and C5-S show the reconstructed fluorescence signal from simulated data using calibrated, estimated, and NIROT-derived optical properties, respectively. A detailed explanation of applied optical maps can be referred to Table 1. Three planes are visualized at the cross position of (30, 30, 11) mm.

More detailed information derived from the reconstructed images are shown in Fig. 6, with its upper panel depicting the profiles along x-, y-, and z-axes and its lower panel showing metrics (CNR, Dice similarity, and MSE) for quantitatively evaluation of reconstruction performance. The profile drawings show that C1-S and C5-S localize the fluorescence signal more accurately than the remainder (Figs. 6(a)–6(c)). For all three quantitative metrics, C1-S achieves the leading score, closely followed by C5-S in each case (Figs. 6(d)–6(f)). For example, the CNR values for C1-S and C5-S are 46.7 and 39.0, respectively, which are much better than the remainder (C2-S, 26.7; C3-S, 10.5; C4-S, 11.6). For the geometrical evaluation, C1-S and C5-S score 0.491 and 0.462, which are more than half the value of the remainder. Putting aside C1-S and C5-S, we find that C2-S leads the ranking in both CNR and Dice similarity, which is in a good agreement with the visual validation in Fig. 5. In summary, both direct visualization of the reconstructed image and secondary analysis show that in the simulation case, reconstruction using NIROT-derived information (C5-S) achieves a similar quality as that using a ground truth value of optical properties (C1-S).

3.3. FMT reconstruction from experimental data

After the simulation, we further investigated the issue of introducing different optical properties in experimental datasets. Figure 7 displays all three planes of reconstructed fluorescence signal

Optics EXPRESS

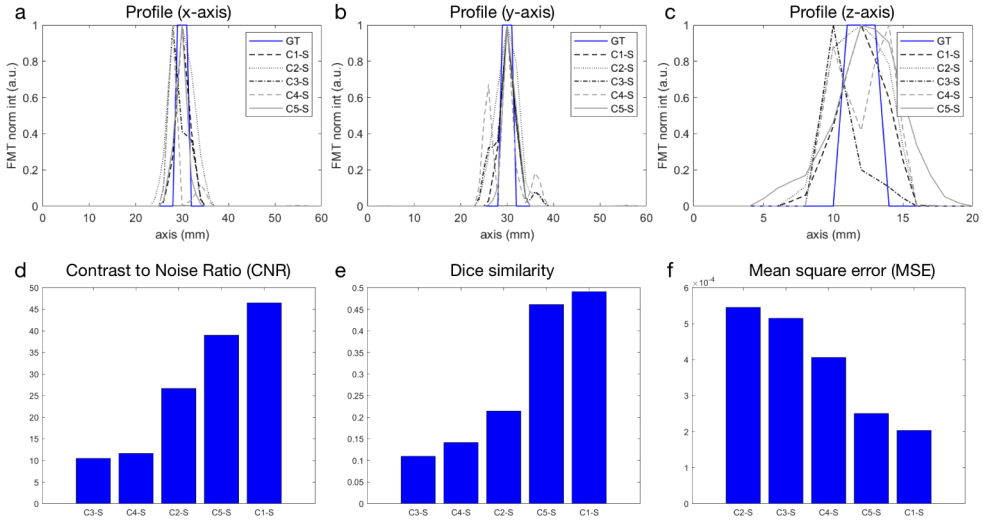

Fig. 6. Images in the upper panel (a-c) show the profiles of the reconstructed fluorescence signal (simulated data) along x-, y-, and z-axes. Blue lines stand for the ground truth. The lower panel includes metrics (CNR, Dice similarity, and MSE) for quantitative evaluation of reconstruction performance in different cases (d-f). A detailed explanation of applied optical maps is displayed in Table 1.

at the cross position of (30, 30, 11) mm for each reconstruction case (C1-C5). Similarly, like in the case of simulation, C1-E using a 'ground truth' map of optical properties can achieve a resolved fluorescence distribution with correct depth information (Fig. 7(b)). In the previous simulation case, C2/C3/C4-S, the reconstruction using 'wrong' maps, can still resolve part of the fluorescence signal. However, in the experimental case, C2/C3/C4-E is not able to reconstruct the correct signal. C2-E can recover the point-like shape of the target and the correct lateral position (in the xy-plane), but it miscalculated the depth information (Fig. 7(c)). C3/C4-E completely fails to perform the reconstruction and generated obvious surface-weighted artifacts in xz- and yz-planes of Figs. 7(d) and 7(e). C5-E incorporating the NIROT-derived optical properties shows a better reconstruction result with the correct shape and position information compared with the ground truth (Fig. 7(f)).

Profile drawings along three axes and quantitative metrics, including CNR, Dice similarity, and MSE, are shown in Fig. 8. Only C1-E and C5-E localize the fluorescence correctly in all three axes (Figs. 8(a)–8(c)). Surprisingly, C5-E shows an even smaller value of full width half maximum (FWHM) in x-, and y-profiles compared with C1-E. As C2/C3/C4-E can not recover the signal, values of CNR and Dice similarity are not applicable (NA). Only C1-E and C5-E score CNR and Dice similarity. For the MSE, we also observe that C5-E outperforms the remainder, including C1-E. Nevertheless, the MSE values for C1-E, C2-E, and C5-E fall into the narrow range of [0.0065, 0.0075], which are very close to each other.

3.4. *Volumetric rendering of fluorescence and optical properties*

In order to obtain a full picture of both NIROT and FMT reconstructions, we have overlaid the fluorescence signal obtained from FMT and optical properties obtained from TD-NIROT for the experimental data (Fig. 9). All volumetric renderings of the isosurfaces were thresholded with a 60% intensity of the maximum value. In the end, our multimodal imaging method resulted in a 3D visualization with three different types of contrast, i.e., fluorescence, absorption, and scattering (Fig. 9(d)).

Optics EXPRESS

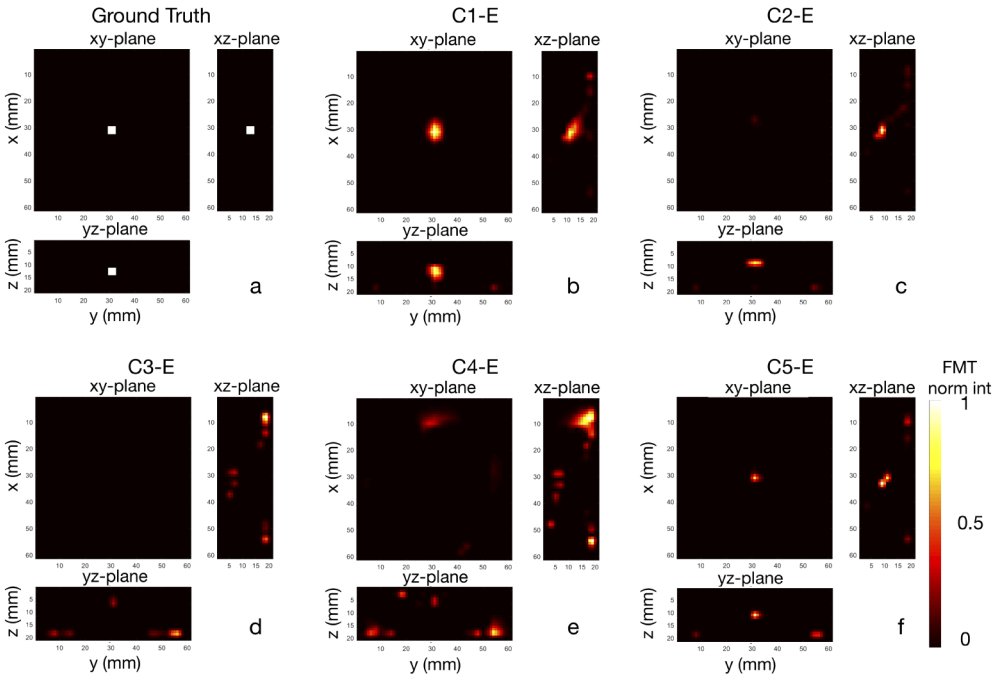

Fig. 7. The reconstructed fluorescence distributions from experimental data using different maps of optical properties (b-f) are compared with the ground truth (a). C1-E, C2/3/4-E, and C5-E show the reconstructed fluorescence signal from experimental data using calibrated, estimated, and NIROT-derived optical properties, respectively. A detailed explanation of applied optical maps is displayed in Table 1. Three planes are visualized at the cross position of (30, 30, 11) mm.

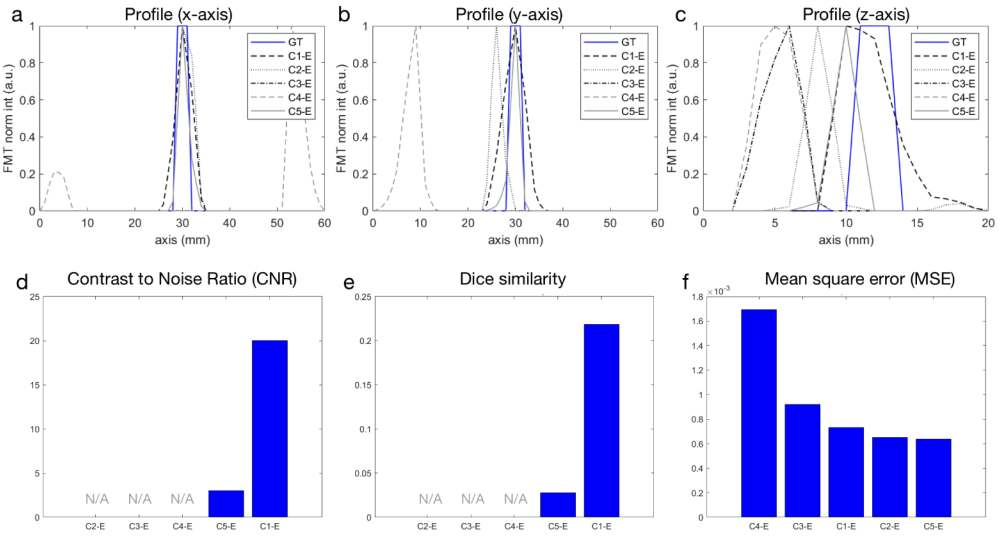

Fig. 8. Images in the upper panel (a-c) show the profiles of the reconstructed fluorescence signal (experimental data) along x-, y-, and z-axes. Blue lines stand for the ground truth. The lower panel includes metrics (CNR, Dice similarity, and MSE) for quantitative evaluation of reconstruction performance in different cases (d-f). A detailed explanation of applied optical maps is displayed in Table 1.

Optics EXPRESS

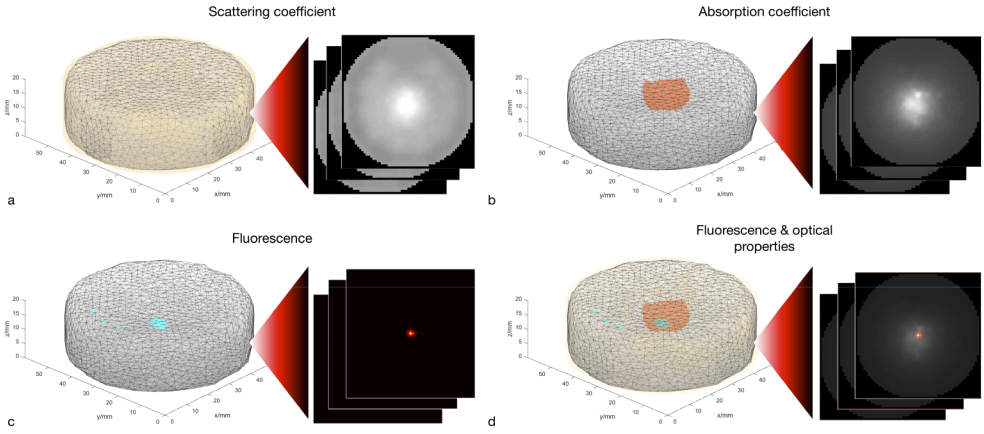

Fig. 9. (a) Scattering coefficient map obtained from NIROT; (b) Absorption coefficient map obtained from NIROT; (c) FMT reconstruction using the optical properties obtained from NIROT; (d) Overlaid image with fluorescence and optical properties. In each type of contrast, the isosurface is thresholded by 60% of the maximum value.

4. Discussion and conclusion

The new-generation SPAD technique not only increases the number of detector-source pairs but also brings valuable time-of-flight information of emitted photons, contributing to a better NIROT reconstruction with decoupled absorption and scattering coefficients when compared with CW method. Figure 4 shows a successful recovery of both optical properties, especially in the aspect of absolute values. The TD-NIROT measurement was followed by CW-FMT, which provides more flexibility during experiments and a high signal-to-noise ratio in raw measurement (the fluorescence signal is low and requires highly sensitive detection). Both simulation and phantom experiments have demonstrated that by plugging in the NIROT-derived optical properties, the FMT reconstruction results are significantly improved and have a comparable quality as the ones by employing calibrated optical properties (Fig. 5 and Fig. 7). As we mentioned in section.2.5, in the experimental part, the reconstruction (C5-E) using NIROT information even outperforms that using calibrated values (C1-E), in the metrics such as FWHM and MSE. There are several possible explanations: 1) the indicated ground truth of fluorescence setting may not reflect the real situation, considering that the amount of injected fluorescent dye and positions of inclusion is difficult to be controlled accurately. 2) the NIROT-derived values can be arguably more close to the phantom's real map of optical properties than the calibration. The calibration procedure of the optical properties of material A and B contains instrumental errors. During FMT reconstruction, the space in the narrow tube was neglected as the FEM-formulation of DE is not applicable in non-diffuse conditions. Considering these factors, the blurred NIROT reconstruction may more accurately help predict the light propagation in the real phantom.

We also further validated the previously reported conclusion that assuming a wrong scattering map will lead to a more negative effect on the reconstruction accuracy when compared with assuming a wrong absorption map [14]. In the simulation case, C2-S using the calibrated scattering coefficient achieves higher values of CNR and Dice similarity than C3-S and C4-S that contains a wrong scattering map. The reconstructed signal in C2-S is more concentrated and centered at a depth of 8-9 mm below the top surface, while the signal in C3-S and C4-S appear more weakly dispersed (Figs. 5(c)–5(e)). In the experimental case, although all reconstruction result using wrong maps failed to recover the correct fluorescence, C2-E shows a concentrated point-like fluorescence target at a depth of 10 mm, which is obviously better than C3-E and C4-E

Optics EXPRESS

with very noisy signal in the middle of the phantom(Figs. 7(c)–7(e)). The predicted target in C2-E is 1-2 mm more in-depth than the ground truth because the absorption map used in the reconstruction is twice higher than the real case.

The combination of FMT and TD-NIROT synergistically enables many advantages. The optical properties obtained from TD-NIROT can not only be used to guide FMT reconstruction as prior information, but also bring crucial functional information about the living tissue. The hemoglobin is the main oxygen transporter and by far the strongest absorbers of NIR light in the tissue. Thus, TD-NIROT enables quantitatively imaging of the the hemoglobin concentration, tissue oxygen saturation, and the fractional blood volume. The oxygenation of tissue is a parameter of tremendous clinical importance in many fields, in particular in oncology. This intrinsic functional information from NIROT excellently complements the molecular information from the fluorescently labeled contrast agents via FMT. One drawback of NIROT is that it is difficult to detect small tumors at early stages [42]. Here, TD-NIROT profits from a combination with FMT, which is highly sensitive to capture low-concentration fluorescence signals specific to tumors if proper probes are selected. Hence the multimodal imaging combining FMT and NIROT is very attractive from many perspectives.

Our multimodal strategy is implemented by conducting FMT and NIROT in a sequential manner, which adds complexity to the operation. A genuinely hybrid TD NIROT-FMT system has to be developed in the future. The principle of both NIROT and FMT relies on diffuse optics. However, the primary contrast of interests and purpose of each modality are different, resulting in different optimization strategies for the device configuration. For instance, data in TD-NIROT containing time-of-flight information is required to decouple scattering and absorption for the whole object. Nevertheless, for FMT, CW measurement provides a high signal-to-noise ratio for low-concentration and sparse fluorescence signal in the living tissue. The camera selection is also different in our case. The currently used SPAD camera for TD-NIROT has an excellent temporal resolution of approximately 100 ps, but only contains 32 x 32 pixels and detection efficiency of about 30% in the near-infrared range. Whereas, a typical fluorescence camera used for non-contact FMT features over 500 x 500 pixels and detection efficiency of over 80%, which guarantees FMT's high sensitivity and flexibility to choose different regions of interests [6]. The next step to implement a hybrid TD NIROT-FMT system is by adopting a dual-camera configuration in a switchable manner or by placing two cameras on opposite sides of the object. Although the detection efficiency of the SPAD camera used here is significantly lower than the CCD camera at near-infrared wavelengths, there are a few technological developments which could close this gap. For example, a microlens array can be manufactured on top of the sensor to focus light onto the pixel array [43], thus increasing the effective pixel fill-factor. Similarly, a next-generation sensor could be produced in a 3D IC technology with the SPAD array and processing electronics on separate dies [44]. This also has the effect of increasing the fill-factor of the sensor but also since the SPADs can now be backside-illuminated they are more sensitive to near-infrared wavelengths. Of course, such a hybrid system would profit from an ideal camera that simultaneously features time-of-flight capability, a large number of detection pixels, and high detection efficiency in the near-infrared wavelength.

In conclusion, we propose a multimodal imaging method combining TD-NIROT and CW-FMT, providing complementary functional and molecular information in the tissue. Both numerical simulation and experiments using a heterogeneous phantom indicate that the scattering and absorption parameters decoupled by TD-NIROT significantly improve the reconstruction quality of FMT via the metrics such as CNR, Dice similarity, and MSE. We also demonstrated that the correct assumption of the scattering coefficient plays a more important role than the absorption coefficient in FMT reconstruction. In the future, we expect more complicated phantom studies and in vivo imaging using mice to optimize the multimodal imaging and further push to its application in drug development and tumor diagnostics.

Optics EXPRESS

Funding

Schweizerischer Nationalfonds zur Förderung der Wissenschaftlichen Forschung (159490, 178262); Horizon 2020 Framework Programme (801347); Ministerio de Economía y Competitividad (FIS2016-77892-R); Krebsforschung Schweiz (KFS-3732-08-2015).

Disclosures

The authors declare that there are no conflicts of interest related to this article.

References

1. V. Ntziachristos, C. H. Tung, C. Bremer, and R. Weissleder, "Fluorescence molecular tomography resolves protease activity in vivo," Nat. Med. **8**(7), 757–761 (2002).
2. M. Rudin, *Molecular imaging: basic principles and applications in biomedical research* (Imperial College Press, 2019).
3. V. Ntziachristos, A. Yodh, M. Schnall, and B. Chance, "Concurrent mri and diffuse optical tomography of breast after indocyanine green enhancement," Proc. Natl. Acad. Sci. **97**(6), 2767–2772 (2000).
4. P. Mohajerani, M. Koch, K. Thurmel, B. Haller, E. J. Rummeny, V. Ntziachristos, and R. Meier, "Fluorescence-aided tomographic imaging of synovitis in the human finger," Radiology **272**(3), 865–874 (2014).
5. M. N. van Oosterom, P. Meershoek, M. M. Welling, F. Pinto, P. Matthies, H. Simon, T. Wendler, N. Navab, C. J. H. van de Velde, H. G. van der Poel, and F. W. B. van Leeuwen, "Extending the hybrid surgical guidance concept with freehand fluorescence tomography," IEEE Trans. Med. Imaging **39**(1), 226–235 (2020).
6. C. Darne, Y. J. Lu, and E. M. Sevick-Muraca, "Small animal fluorescence and bioluminescence tomography: a review of approaches, algorithms and technology update," Phys. Med. Biol. **59**(1), R1–R64 (2014).
7. S. R. Arridge and J. C. Schotland, "Optical tomography: forward and inverse problems," Inverse Probl. **25**(12), 123010 (2009).
8. J. Ripoll, *Principles of diffuse light propagation: light propagation in tissues with applications in biology and medicine* (World Scientific, 2012).
9. J. Ripoll and V. Ntziachristos, "From finite to infinite volumes: removal of boundaries in diffuse wave imaging," Phys. Rev. Lett. **96**(17), 173903 (2006).
10. S. R. Arridge, M. Schweiger, M. Hiraoka, and D. T. Delpy, "A finite element approach for modeling photon transport in tissue," Med. Phys. **20**(2), 299–309 (1993).
11. R. Yao, X. Intes, and Q. Q. Fang, "Generalized mesh-based monte carlo for wide-field illumination and detection via mesh retessellation," Biomed. Opt. Express **7**(1), 171–184 (2016).
12. Q. Q. Fang and D. A. Boas, "Monte carlo simulation of photon migration in 3d turbid media accelerated by graphics processing units," Opt. Express **17**(22), 20178–20190 (2009).
13. H. Dehghani, S. Srinivasan, B. W. Pogue, and A. Gibson, "Numerical modelling and image reconstruction in diffuse optical tomography," Philos. Trans. R. Soc., A **367**(1900), 3073–3093 (2009).
14. J. F. P.-J. Abascal, J. Aguirre, J. Chamorro-Servent, M. Schweiger, S. Arridge, J. Ripoll, J. J. Vaquero, and M. Desco, "Influence of absorption and scattering on the quantification of fluorescence diffuse optical tomography using normalized data," J. Biomed. Opt. **17**(3), 036013 (2012).
15. V. Ntziachristos and R. Weissleder, "Experimental three-dimensional fluorescence reconstruction of diffuse media by use of a normalized born approximation," Opt. Lett. **26**(12), 893 (2001).
16. T. Pyka, R. Schulz, A. Ale, and V. Ntziachristos, "Revisiting the normalized born approximation: effects of scattering," Opt. Lett. **36**(22), 4329 (2011).
17. D. Hyde, R. de Kleine, S. A. MacLaurin, E. Miller, D. H. Brooks, T. Krucker, and V. Ntziachristos, "Hybrid fmt-ct imaging of amyloid-beta plaques in a murine alzheimer's disease model," NeuroImage **44**(4), 1304–1311 (2009).
18. F. Stuker, C. Baltes, K. Dikaiou, D. Vats, L. Carrara, E. Charbon, J. Ripoll, and M. Rudin, "Hybrid small animal imaging system combining magnetic resonance imaging with fluorescence tomography using single photon avalanche diode detectors," IEEE Trans. Med. Imaging **30**(6), 1265–1273 (2011).
19. W. Ren, H. Isler, M. Wolf, J. Ripoll, and M. Rudin, "Smart toolkit for fluorescence tomography: simulation, reconstruction, and validation," IEEE Trans. Biomed. Eng. **67**(1), 16–26 (2020).
20. W. Ren, A. Elmer, D. Buehlmann, M.-A. Augath, D. Vats, J. Ripoll, and M. Rudin, "Dynamic measurement of tumor vascular permeability and perfusion using a hybrid system for simultaneous magnetic resonance and fluorescence imaging," Mol. Imaging Biol. **18**(2), 191–200 (2016).
21. W. Ren, A. Elmer, M.-A. Augath, and M. Rudin, "Fem-based simulation of a fluorescence tomography experiment using anatomical mr images," in *Medical Imaging 2016: Biomedical Applications in Molecular, Structural, and Functional Imaging*, vol. 9788 (International Society for Optics and Photonics, 2016), p. 978828.
22. S. L. Jacques, "Optical properties of biological tissues: a review," Phys. Med. Biol. **58**(11), R37–R61 (2013).
23. T. Lister, P. A. Wright, and P. H. Chappell, "Optical properties of human skin," J. Biomed. Opt. **17**(9), 0909011 (2012).

Optics EXPRESS

24. M. N. Polatoglu, Y. Liu, R. Ni, J. Ripoll, M. Rudin, M. Wolf, and W. Ren, "Simulation of fluorescence molecular tomography using a registered digital mouse atlas," in *Diffuse Optical Spectroscopy and Imaging VII*, vol. 11074, (International Society for Optics and Photonics, 2019), p. 110740C.
25. A. Gibson and H. Dehghani, "Diffuse optical imaging," Philos. Trans. R. Soc., A **367**(1900), 3055–3072 (2009).
26. Y. Y. Tan and H. B. Jiang, "Diffuse optical tomography guided quantitative fluorescence molecular tomography," Appl. Opt. **47**(12), 2011–2016 (2008).
27. Y. Tan, Z. Cao, H. K. Sajja, M. Lipowska, Y. A. Wang, L. Yang, and H. Jiang, "Dot corrected fluorescence molecular tomography using targeted contrast agents for small animal tumor imaging," J. X-Ray Sci. Technol. **21**(1), 43–52 (2013).
28. Y. Lin, H. Yan, O. Nalcioglu, and G. Gulsen, "Quantitative fluorescence tomography with functional and structural a priori information," Appl. Opt. **48**(7), 1328 (2009).
29. T. Correia, N. Ducros, C. D'Andrea, M. Schweiger, and S. Arridge, "Quantitative fluorescence diffuse optical tomography in the presence of heterogeneities," Opt. Lett. **38**(11), 1903 (2013).
30. S. R. Arridge and W. R. B. Lionheart, "Nonuniqueness in diffusion-based optical tomography," Opt. Lett. **23**(11), 882 (1998).
31. M. D. Wheelock, J. P. Culver, and A. T. Eggebrecht, "High-density diffuse optical tomography for imaging human brain function," Rev. Sci. Instrum. **90**(5), 051101 (2019).
32. V. Ntziachristos, A. G. Yodh, M. Schnall, and B. Chance, "Concurrent mri and diffuse optical tomography of breast after indocyanine green enhancement," Proc. Natl. Acad. Sci. U. S. A. **97**(6), 2767–2772 (2000).
33. A. Kalyanov, J. Jiang, S. Lindner, L. Ahnen, A. Costanzo, J. Pavia, S. Majos, and M. Wolf, "Time domain near-infrared optical tomography with time-of-flight spad camera: The new generation," in *Optical Tomography and Spectroscopy*, (Optical Society of America, 2018).
34. S. Lindner, C. Zhang, I. Antolovic, A. Kalyanov, J. Jiang, L. Ahnen, A. Costanzo, J. Pavia, S. Majos, E. Charbon, and M. Wolf, "A novel 32× 32, 224 mevents/s time resolved spad image sensor for near-infrared optical tomography," in *Biophotonics Congress: Biomedical Optics Congress*, (Optical Society of America, 2018).
35. W. Ren, "Stift: a modular software platform for simulation, optimization and reconstruction in fluorescence molecular tomography," Ph.D. thesis, ETH Zurich, (2018).
36. N. Tomm, L. Ahnen, H. Isler, S. Kleiser, T. Karen, D. Ostojic, M. Wolf, and F. Scholkmann, "Characterization of the optical properties of color pastes for the design of optical phantoms mimicking biological tissue," J. Biophotonics **12**(4), e201800300 (2019).
37. D. M. Hueber, S. Fantini, A. E. Cerussi, and B. B. Barbieri, "New optical probe designs for absolute (self-calibrating) nir tissue hemoglobin measurements," in *Optical tomography and spectroscopy of tissue III*, vol. 3597, (International Society for Optics and Photonics, 1999), pp. 618–631.
38. H. Dehghani, M. E. Eames, P. K. Yalavarthy, S. C. Davis, S. Srinivasan, C. M. Carpenter, B. W. Pogue, and K. D. Paulsen, "Near infrared optical tomography using nirfast: Algorithm for numerical model and image reconstruction," Commun. Numer. Meth. Engng. **25**(6), 711–732 (2009).
39. J. Jiang, L. Ahnen, A. Kalyanov, S. Lindner, M. Wolf, and S. S. Majos, "A new method based on graphics processing units for fast near-infrared optical tomography," Adv. Exp. Med. Biol. **977**, 191–197 (2017).
40. Q. Fang and D. A. Boas, "Tetrahedral mesh generation from volumetric binary and grayscale images," in *2009 IEEE International Symposium on Biomedical Imaging: From Nano to Macro*, (Ieee, 2009), pp. 1142–1145.
41. M. Schweiger and S. R. Arridge, "The toast++ software suite for forward and inverse modeling in optical tomography," J. Biomed. Opt. **19**(4), 040801 (2014).
42. A. Konovalov, E. Genina, and A. Bashkatov, "Diffuse optical mammotomography: state-of-the-art and prospects," J. Biomed. Photonics Eng. **1**, 020202-1 (2016).
43. I. M. Antolovic, A. C. Ulku, E. Kizilkan, S. Lindner, F. Zanella, R. Ferrini, M. Schnieper, E. Charbon, and C. Bruschini, "Optical-stack optimization for improved spad photon detection efficiency," in *Quantum Sensing and Nano Electronics and Photonics XVI*, vol. 10926 (International Society for Optics and Photonics, 2019), p. 109262T.
44. J. M. Pavia, M. Scandini, S. Lindner, M. Wolf, and E. Charbon, "A 1× 400 backside-illuminated spad sensor with 49.7 ps resolution, 30 pj/sample tdcs fabricated in 3d cmos technology for near-infrared optical tomography," IEEE J. Solid-State Circuits **50**(10), 2406–2418 (2015).